



UNIVERSITY OF LEEDS

This is a repository copy of *Monte Carlo method for the analysis of laser safety for a high-powered lidar system under different atmospheric conditions*.

White Rose Research Online URL for this paper:
<http://eprints.whiterose.ac.uk/113519/>

Version: Accepted Version

Article:

Stillwell, R, Pilewskie, P, Thayer, J et al. (2 more authors) (2017) Monte Carlo method for the analysis of laser safety for a high-powered lidar system under different atmospheric conditions. *Journal of Laser Applications*, 29 (2). 022002. ISSN 1042-346X

<https://doi.org/10.2351/1.4977483>

(c) 2017, Laser Institute of America. This is an author produced version of a paper published in the *Journal of Laser Applications*. Uploaded in accordance with the publisher's self-archiving policy.

Reuse

Unless indicated otherwise, fulltext items are protected by copyright with all rights reserved. The copyright exception in section 29 of the Copyright, Designs and Patents Act 1988 allows the making of a single copy solely for the purpose of non-commercial research or private study within the limits of fair dealing. The publisher or other rights-holder may allow further reproduction and re-use of this version - refer to the White Rose Research Online record for this item. Where records identify the publisher as the copyright holder, users can verify any specific terms of use on the publisher's website.

Takedown

If you consider content in White Rose Research Online to be in breach of UK law, please notify us by emailing eprints@whiterose.ac.uk including the URL of the record and the reason for the withdrawal request.



eprints@whiterose.ac.uk
<https://eprints.whiterose.ac.uk/>

Monte Carlo Method for the Analysis of Laser Safety for a High-Powered Lidar System under Different Atmospheric Conditions

Robert A. Stillwell,¹ Peter Pilewski,^{2,3} Jeffrey P. Thayer,¹ Michael O'Neill,⁴ and Ryan R. Neely III^{4,5,6}

¹*Aerospace Engineering Sciences, University of Colorado at Boulder, ECNT 320, 431 UCB, University of Colorado, Boulder, CO 80309*

²*Atmospheric and Oceanic Sciences Department, University of Colorado at Boulder, 311 UCB, University of Colorado, Boulder, CO 80309*

³*Laboratory for Atmospheric and Space Physics, University of Colorado at Boulder, 1234 Innovation Drive, Boulder, CO 80303*

⁴*Cooperative Institute for Research in Environmental Sciences, University of Colorado at Boulder, 216 UCB, University of Colorado, Boulder, CO 80309*

⁵*School of Earth and Environment, The University of Leeds, Leeds, LS2 9JT, United Kingdom*

⁶*National Centre for Atmospheric Science, University of Leeds, Leeds, UK*

(Dated: 14 March 2017)

A major concern of high-powered atmospheric lidar systems is eye safety. Atmospheric lidars are often run unattended in adverse weather conditions where scattering redirects laser energy from the main beam. These naturally varying “soft targets” (such as fog and precipitation) are not accounted for in ANSI standards but, through multiple scattering events, can potentially create adverse viewing conditions. This paper introduces a Monte Carlo method that uses scattering phase functions for fog and snow and applies multiple scattering analysis to map the energy density within a scattering volume around the primary beam. Careful attention is given to accurately describing the forward scattering portion of the phase function as it scatters a significant amount of the beam energy. This method is compared to ANSI standard hazard zone calculations to determine what effect scattering has on the size of the hazard zone. For direct beam viewing, hazard zone size estimates are within about 3% of the ANSI defined Nominal Ocular Hazard Distance (NOHD) for clear air but are approximately 56% smaller than the NOHD as optical density increases for scattering in fog and approximately 33% smaller for scattering in blowing snow. For indirect beam exposure, clear air gives the worst approximation to the ANSI defined Nominal Hazard Zone (NHZ), in error by approximately 95%; fog approaches the ANSI results, within 28%, whereas blowing snow shows only 68% agreement. Finally, scattering enhancement mechanisms are considered which relate to the definition of the scattering layer of interest and increase scattered energy density observed by approximately 4%. In all cases, the ANSI calculated NOHD and NHZ are larger than the hazard zones that include scattering but the size of the zones is inextricably linked to the type of scattering ignored in the standard NOHD and NHZ calculations.

Keywords: Lidar, Laser Safety, Monte Carlo, Multiple Scattering, Arctic, Polar

I. INTRODUCTION

Atmospheric observations by lidars present many benefits for the atmospheric science community. Lidars are capable of directly or indirectly measuring many state variables that are critically important in understanding atmospheric processes. Among these state variables, lidar is adept at measuring temperature, line of sight wind, constituent mixing ratios, aerosol optical depth, and cloud properties to name a few¹⁻³. Further advantages are enabled by deploying lidar systems that can operate continuously and autonomously in remote locations⁴⁻⁶. These measurements all place different constraints on lidar system specifications such as laser line width, power, repetition rate, and wavelength¹⁻¹¹. These measurement constraints must be examined within the context of laser safety to ensure that the benefit of lidar to the atmospheric science community is not outweighed by the potential hazards of deploying and operating such systems.

For ground-based lidar systems that lack steering and are directed vertically, direct beam exposure is a concern for aircraft/spacecraft as well as personnel working near the system. The American National Standards Institute (ANSI), in an attempt to standardize and regulate the vast array of laser systems, defines limits of exposure to which one can be safely subjected¹². Careful attention must be paid to ensure that at no point can human exposure to laser light exceed the Maximum Permissible Exposure (MPE), which is a function of laser characteristics such as wavelength, peak power, pulse repetition rate, pulse width, and exposure time. Using the MPE and beam characteristics, the Nominal Ocular Hazard Distance (NOHD) and Nominal Hazard Zone (NHZ) can be calculated, which assume no scattering for the NOHD and complete Lambertian scattering for the NHZ. It is crucial to note however that atmospheric conditions can lead to indirect exposure through scattering that fits neither standard calculation type.

Ensuring laser safety for atmospheric lidar is uniquely challenging due to designs requiring high peak power, short pulses, and output wavelengths near the visible portion of the spectrum. Furthermore, for atmospheric lidar, the beam cannot be fully enclosed after it leaves the building. The beam is most readily accessible in the atmosphere, but the ANSI standard description of the propagation medium is simplified by not accounting for partial scattering through the propagation medium^{12,13}. This paper considers the effect of atmospheric scattering and quantifies the change in the hazard zone size compared to the NOHD

and NHZ as a function of common atmospheric scattering regimes like clear air, fog and blowing snow.

This paper introduces a method whereby one can test whether the directly transmitted and scattered energy density in the vicinity of a high-energy laser beam propagating through an atmosphere meets all necessary MPE values. A ground-based, autonomous atmospheric lidar system under development, whose goal of profiling atmospheric water vapor and temperature requires high-energy laser light to propagate through the atmosphere, will serve as the system under study. The goal of this work is to map the energy density of the direct (unscattered and near-zero deviation forward scattering) and indirect (scattered out of the main beam) laser beam as it propagates through a diverse atmosphere as a function of 3-D space where humans could encounter it. Using a Monte Carlo method to account for scattering and propagation processes, a statistical map of energy density is calculated. Of interest is to define a hazard zone, outside of which, one can guarantee the direct and indirect beam will be below the relevant MPE, akin to the ANSI defined NOHD and NHZ, and to compare the resultant hazard zone to the NOHD and NHZ to determine the effect atmospheric scattering has on the size and shape of this region.

The outline of this paper is as follows. An overview of the techniques used to implement the Monte Carlo scheme to model atmospheric processes is given in Section II. Relevant scattering characteristics for the test system are introduced with an emphasis on how to include such characteristic into the Monte Carlo method in Section III. A short overview of the test lidar system as well as ANSI standard NOHD and NHZ calculations are provided in Section IV. Three case studies of atmospheric scattering are presented in Section V which are compared to the NOHD and NHZ standard calculations in Section VI. The paper ends with a summary and conclusion in Section VII.

II. MONTE CARLO METHODS

Transfer of radiation in complicated multi-scattering media can be solved in a statistical manner to produce solutions that converge to exact solutions given large numbers of modeled events. In the case of radiation propagation in the atmosphere, statistical methods can be used to model absorption and scattering especially considering multiple scattering¹⁴. The Monte Carlo technique is a statistical method that leverages random sampling techniques

to understand problems containing multiple probabilistic events¹⁵. The goal of this work is to model the propagation of photons through the atmosphere and map their locations as they exit a layer of interest to understand the effect atmospheric targets, i.e. “soft targets”, can have on the hazard zone definition. The Monte Carlo method is well equipped for this sort of study because it can robustly handle optically thick media, multiple scattering media, without a priori constraint on the number of scattering events. The following sections describe the basic outline of the Monte Carlo simulations; the reader is referred to several works for further information on creating such simulations and for information on variance reduction techniques^{14,16–20}.

A. Weighted Random Numbers

One critical element of implementing a Monte Carlo simulation is developing a method to produce weighted random numbers. In this case, several weighted random numbers are needed in the initialization and propagation of photons. The starting location of a photon within the beam, the photon ray angle, the propagation distance before interaction, the probability of scattering versus absorption, and the scattering angle are all needed. A general method is to constrain the probability density of a function such that it obeys Equation 1^{14,15}. Here μ is any variable for which a weighted random number is desired, ξ is a randomly generated number from a uniform probability distribution, and p is the continuous probability density of the desired variable. For functions that can be easily integrated and inverted, optical depth being one example, this method is straightforward and robust. The integration yields the functional dependence; all that is needed is the specification of boundary conditions.

$$\int p(\mu) d\mu = \int 1 d\xi \quad (1)$$

The probability density of a photon propagating at an optical depth, τ , before scattering is simply $p(\tau) = \exp(-\tau)$. Integrating this and matching the boundary conditions, $\xi = 0$ where $\tau = 0$ yields a weighting function of optical depth. This is given in Equation 2.

$$\tau(\xi) = -\ln(1 - \xi) \quad (2)$$

For functions that do not possess a simple closed form to this integral, this method is

impractical. An example of such a function is a phase function calculated directly from Mie theory. A second is a phase function calculated from an improved geometric optics method²¹, which does not have a closed form representation. Furthermore, simple functions, which can be integrated but result in equations that can not be inverted to yield a μ dependence as a function of ξ are also problematic. An example of this is the small particle scattering phase function, the Rayleigh phase function, which yields an equation of the form $\mu + \sin(\mu) = \xi$.

One method to solve this problem is to approximate the scattering phase function with analytic functions that match some of the general characteristics. For the phase functions mentioned, the Henyey-Greenstein function is commonly used^{14,19,20,22-24}. It can be exactly integrated and a weighted random number can be specified as a function of the random number generated, ξ . The Henyey-Greenstein phase function cannot match several of the characteristics exhibited in real scattering phase functions, such as the forward and backward peaks, or the rainbow, so numerical solutions are required for improved accuracy. Furthermore, the results shown below will demonstrate that exact treatment of the phase function, and in particular the representation of the prominent forward scattering peak, is critical to laser safety applications and can strongly impact the resultant energy density maps.

B. Coordinate Representation

To create a map of energy density at specified locations, one needs a method to track the motion of a photon through a layer of interest. The scattering phenomena to be modeled are expressed in spherical coordinates. The angle from zenith, θ , for a scattering event can be directly calculated from the phase function of the scatterer and the azimuth angle, ϕ , is defined as a uniform probability distribution when scattering is azimuthally symmetric, as it is for spheres and randomly oriented particles. With these two angles, the direction of propagation of the i^{th} propagation is defined in Equation 3.

$$\bar{\Omega}_i = \begin{bmatrix} \sin(\theta_i) \cos(\phi_i) \\ \sin(\theta_i) \sin(\phi_i) \\ \cos(\theta_i) \end{bmatrix} \quad (3)$$

Each scattering event is referenced to a unique reference frame. It is noted that vectors referenced to different frames cannot be simply added. The z-axis of each frame is determined

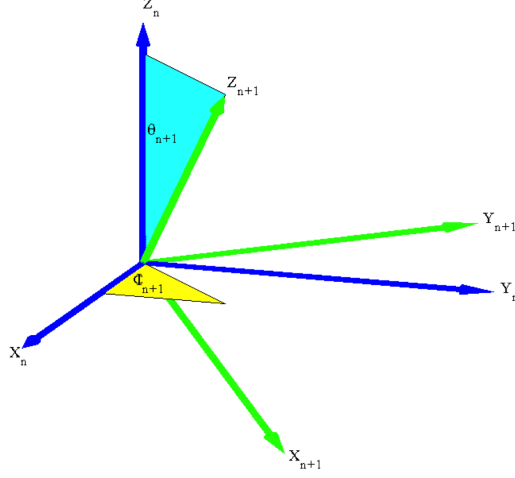


FIG. 1. A representation of the scattering angles needed to define the propagation orientation after scattering. The original coordinates are taken with the propagation direction along the z-axis. These angles are used to define scattering and to rotate new propagation vectors back to a standard coordinate system.

by the previous scattering vector. A definition of the vector in terms of a common coordinate system is required to track the photon. To link the vectors, a system of rotation matrices is used. This system can be derived from general Cartesian rotation matrices, which is generated from two of the three basic 3 dimensional rotations, given in Equation 4²⁵.

$$R_y(\beta) = \begin{bmatrix} \cos(\beta) & 0 & -\sin(\beta) \\ 0 & 1 & 0 \\ \sin(\beta) & 0 & \cos(\beta) \end{bmatrix} \tag{4}$$

$$R_z(\delta) = \begin{bmatrix} \cos(\delta) & \sin(\delta) & 0 \\ -\sin(\delta) & \cos(\delta) & 0 \\ 0 & 0 & 1 \end{bmatrix}$$

Combining a rotation about the y-axis with a rotation about the z-axis is sufficient to define the scattering events. This combination is given in Equation 5 and shown in Figure 1. This matrix is used to link the propagation vector before and after scattering. It is useful to construct this matrix relationship from basic rotations because the basic rotations are orthonormal matrices. This implies that the matrix is invertible and that the inverse of the matrix can be expressed as the transpose of the matrix²⁵.

$$\bar{M}_i = R_y(\theta_i) R_z(\phi_i) = \begin{bmatrix} \cos(\theta_i) \cos(\phi_i) & \cos(\theta_i) \sin(\phi_i) & -\sin(\theta_i) \\ -\sin(\phi_i) & \cos(\phi_i) & 0 \\ \sin(\theta_i) \cos(\phi_i) & \sin(\theta_i) \sin(\phi_i) & \cos(\theta_i) \end{bmatrix} \quad (5)$$

In this way, the location of the photon within the layer of interest, ζ , can always be linked back to some specified coordinate system by performing rotations back to the original reference frame. Furthermore, the vector defined in Equation 3 is simply the z-direction before and after scattering. The general transformation is given in Equation 6.

$$\begin{aligned} \zeta_n &= \bar{M}_{n-1}(\theta_{n-1}, \phi_{n-1}) \zeta_{n-1} \text{ or} \\ \bar{M}_{n-1}^{-1}(\theta_{n-1}, \phi_{n-1}) \zeta_n &= \zeta_{n-1} \end{aligned} \quad (6)$$

C. Photon Propagation

After coordinate system transformations, the location of a photon within a layer is simply the vectorial addition of all of the individual propagation legs. Note that the rotation matrix in Equation 5 connects the old coordinate system to the new so to map a vector in the newest scattering system into an original system, the matrix inverse, or transpose since it is orthonormal, is required. The location of the photon after n scattering events is given in general in Equation 7 where τ_i is the distance traveled on the i^{th} leg calculated from randomly sampling Equation 2 and \bar{M} is the rotation matrix defined in Equation 5 with sampling defined by randomly sampling the scattering phase function. It is of note that $\bar{\Omega}_1$ given in Equation 3 is simply calculated as $\bar{\Omega}_1 = \bar{M}_1^{-1}(\theta_1, \phi_1) \bar{\Omega}$. The matrix multiplications in Equation 7 are defined to be right multiplications and are not commutative.

$$\bar{\tau} = \sum_{i=1}^n \tau_i \left[\prod_{j=1}^i \bar{M}_j^{-1}(\theta_j, \phi_j) \right] \bar{\Omega} \quad (7)$$

Using the above defined random sampling techniques and propagation matrices, a photon can be tracked throughout a layer of interest. If one can accurately represent scattering phenomena, the above mechanics can be used to map all laser photons and track energy density. This allows for one to include any type of scattering phenomena desired and to map locations where energy density exceeds the MPE, facilitating a comparison between safe zones calculated with and without atmospheric scattering and extinction.

III. SCATTERING CHARACTERISTICS

Crucial to the accuracy of the Monte Carlo representation of the laser system is the representation of the characteristics of the propagation medium including absorption and scattering. In this paper only scattering is considered because the single scattering albedo of water and ice at the wavelengths of interest is very nearly 1, to within 10^{-5} . No atmospheric scattering is commonly assumed of the propagating laser beam; the NOHD and NHZ are calculated from the beam characteristics and propagation distance alone for vertical beams regardless of the atmospheric conditions. ANSI 136.6 Appendix C.4 requires atmospheric attenuation corrections for horizontal beams, therefore not calculated for a vertical beam, but also includes the caveat that propagation is for good visibility and no cloud cover¹³. In the case of a top hat beam (near uniform fluence), the NHZ is also the expanded size of the beam required to have no beam energy higher than the MPE. The NOHD and NHZ define a cylindrical region, which if impinged upon would represent a safety hazard. This paper will examine the definition of this region and its change as the optical depth per meter of the propagation medium increases thus increasing the amount of scattering.

Here, the scattering medium is represented in terms of optical depth rather than geometric depth. By performing a conversion of the coordinate axes used, a quantitative comparison of different conditions such as 100 *km* of clear air to 50 *m* of dense fog may be done more effectively. What is desired is a map of energy density, which has units of laser energy per area. This can be calculated by converting Monte Carlo photons per unit square optical depth, making it straightforward to compare different atmospheric conditions quantitatively.

A. Optical Depth

Equation 2 gives the optical depth traveled by a photon before scattering as a function of the random number ξ . One can verify this equation by plotting the theoretical probability density along with the Monte Carlo simulations. In the style of Bohren and Clothiaux¹⁴, the values of τ are discretized into a set number of bins, which are incremented by one each time a Monte Carlo event produces a value in that bin. The results of this process are given in Figure 2 with 5 different numbers of photons with 500 bin discretization over the range $0 \leq \tau \leq 5$.

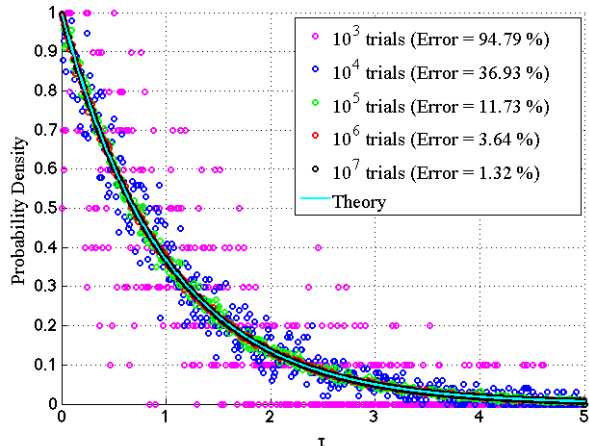


FIG. 2. The continuous probability distribution function $p = \exp(-\tau)$ and its Monte Carlo representation in the style of Bohren and Clothiaux¹⁴. The Monte Carlo representation is computed from calculating weighted random numbers. The axis from $\tau = 0$ to $\tau = 5$ is discretized into 500 equal sized bins. The five different approximations yield a given number of weighted random numbers that are lumped into the bin, which contains it. The average percent error for each of the 500 bins compared to the known probability distribution is given in the legend.

Using the definition in Equation 2, the distance photons travel within a layer of interest before a scattering event occurs is modeled. All that is required is to understand how optical path is related to geometric path. Converting back and forth can be done easily because both coordinates monotonically increase upward from the ground and outwards from the origin. The only complication arises from numerical round-off error when very small regions are selected, for example 10 cm by 1 m . One needs to verify that the numerical calculations performed carry adequate significant digits to capture small distances traveled.

B. Phase Function

Commonly, the scattering phase function is approximated by simple phase functions that can be directly integrated in Equation 1. One such phase function is the Henyey-Greenstein phase function^{24,26}. While it has no physical basis, it broadly resembles the phase functions calculated from Mie theory for spheres and geometric ray tracing codes or T-Matrix algorithms for non-spherical large particles. The forward scattering peak is approximate for small size parameters, but more importantly, the function has a simple integral that can be

inverted. The drawback of this function is that it poorly captures forward and backscattering for large size parameters or other features such as the rainbow from spherical droplets and halos from hexagonal ice. Modifications such as a double Henyey-Greenstein phase function have been suggested but the system becomes impossible to invert to a function of a random variable. A further modification is proposed by Cornette and Shanks²³, which captures more reasonable forward and backscattering behavior especially for smaller particles. Even this more complicated function fails to capture some of the prominent features like the rainbow angle for spheres or the halo in hexagonal ice crystals.

One method for handling real phase functions is to use the normalized cumulative distribution function of a phase function to create weighted random numbers and to solve Equation 1 numerically²⁴. The method can be used to capture all the features of phase functions calculated via Mie theory or ray tracing. The cumulative distribution becomes a lookup table to convert a random number to a scattering direction. This method is more computationally expensive than the method used for the optical depth but is simple and robust to implement and has the advantage that the continuous scattering function can be arbitrarily complicated. A simple phase function is the Rayleigh scattering phase function. It is known analytically but it cannot be inverted like the Henyey-Greenstein phase function or optical depth probability distribution. This method is first demonstrated on the simplest phase function used for the analysis to come. It is given in Figure 3.

A second example of a relevant phase function is for fog, with its Monte Carlo representation and cumulative distribution given in Figure 4. One can see that there exists a unique relationship between cumulative probability (right ordinate), and scattering angle (top abscissa), yielding a procedure for deriving the latter with a random number. Following a similar binning procedure to that given for Figure 2, one can represent complicated phase functions well. The only difference between this phase function and the Rayleigh phase function is that this phase function, due to the large dynamic range, needs to have many points to represent the forward scattering peak. This can be done by using many evenly spaced points or varying resolution for the forward and backscattering peaks. An example of a phase function calculated with evenly spaced points is given in Figure 4.

An example of a phase function calculated with higher resolution in the forward scattering peak is shown in Figure 5. The utility of this method, being that it handles both uniformly and non-uniformly tabulated phase functions, is that one need not calculate the

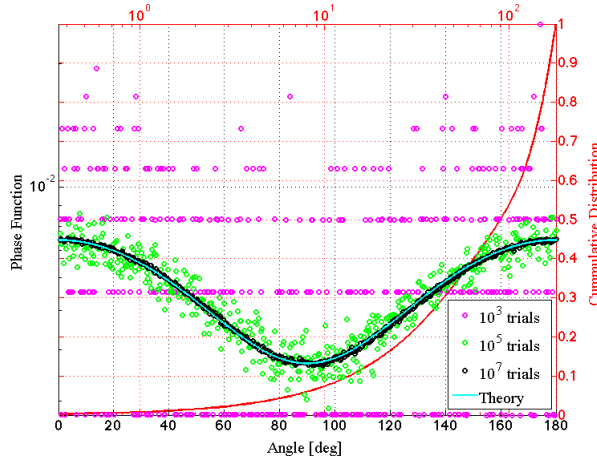


FIG. 3. The continuous probability distribution function for a small dipole scatterer, commonly referred to as Rayleigh scattering. This phase function shows the known dependence in scattering angle, given in the solid cyan line where the function is proportional to cosine, $P(\theta) \propto 1 + \cos(\theta)$. Again multiple trials are run to demonstrate the approximate number of photons required to adequately capture the phase functions information. Note that the top abscissa is logarithmic while the bottom is linear. This is used to show the detail in the forward scattering peak.

function but can use the libraries compiled from ray tracing methods²¹. There is no rigid requirement on how the function need be calculated as long as the forward scattering peak is well represented. Non-uniform resolution in the phase functions can save computation time and increase memory efficiency.

IV. SYSTEM CHARACTERISTICS

To link to the Monte Carlo simulations, the specifications of the high-powered lidar system are provided in Table I. These specifications are common to atmospheric lidar systems, including upper atmospheric Rayleigh lidars like the ones described by Thayer et al. and von Zahn et al.^{10,11} and lower atmospheric Raman systems described by Goldsmith et al. and Di Girolamo et al.^{4,7}. The system to be analyzed is a lower atmospheric Raman lidar system designed to continuously measure water vapor and temperature in the lower atmosphere.

With these specifications in Table I, the Monte Carlo results can be linked to the lidar system. The number of photons produced per pulse is approximately 7×10^{17} . Simulations

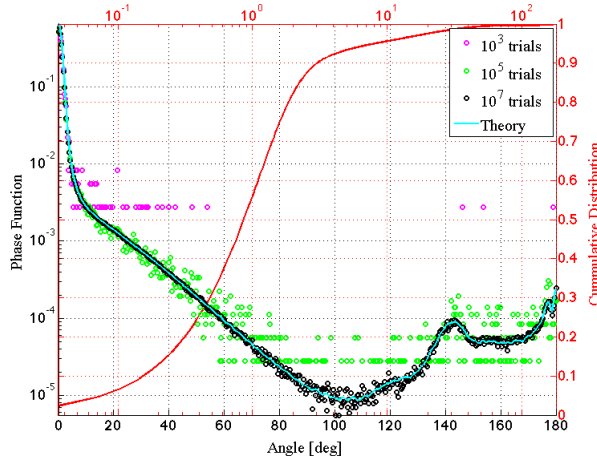


FIG. 4. The continuous probability distribution function for liquid water and its Monte Carlo representation in the style of Bohren and Clothiaux¹⁴. The phase function is calculated using the Mie development given in Bohren and Huffman²⁷ assuming a gamma distribution of spherical particles with an average size of $10 \mu m$. The wavelength of interest is $355 nm$ and the optical properties of water at that wavelength are used as compiled by Warren²⁸. The Monte Carlo representation is computed from calculating weighted random numbers. The axis from $\theta = 0^\circ$ to $\theta = 180^\circ$ is discretized into 500 equal sized bins. The summing is done as in Figure 2 but due to the large change in order of magnitude of the function, many more Monte Carlo trials are required to yield a reasonable match to the true phase function in the $100^\circ \leq \theta \leq 120^\circ$ region.

are run with 1×10^7 Monte Carlo photons, sufficient for statistical convergence. This means that each Monte Carlo photon will represent approximately 7×10^{10} laser photons per pulse. Additionally, the starting location and entrance angle of the photon within the layer is also given by the beam characteristics. The starting location will be randomly distributed within a circle, a top hat beam, of radius $2.7 cm$ with starting angles given by a uniformly distributed number $0 \leq \theta \leq 167 \mu rad$ with an azimuth angle $0 \leq \phi \leq 2\pi rad$. The top hat beam shape is correct for the assumed laser, a commercially available Continuum Model 9030 Nd:YAG laser. Additionally, based on the laser, the beam has been expanded within the transmitting system by a factor of 3.

It should be noted that most atmospheric lidar beams are slightly diverging, but for beams focused at a certain distance, Monte Carlo techniques must account for beam diffraction. If not considered, beams can be modeled to focus to an area smaller than the diffraction limit.

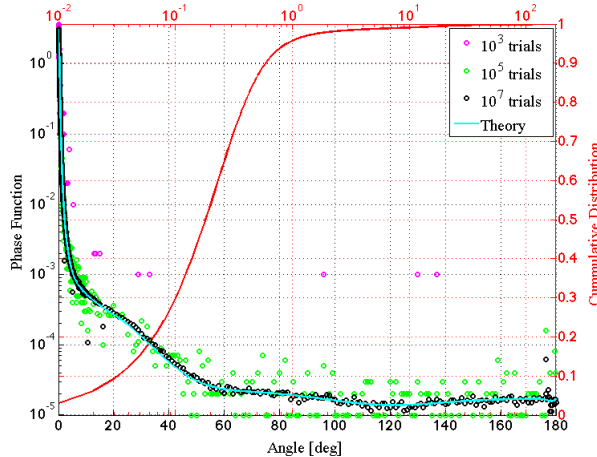


FIG. 5. The continuous probability distribution function for a severely roughened mixed set of ice crystal habits and its Monte Carlo representation in the style of Bohren and Clothiaux¹⁴ as calculated by Yang et al.²¹. The phase function is calculated using a wavelength of light of 355 nm with a mean size of $30\ \mu\text{m}$. The Monte Carlo representation is computed from calculating weighted random numbers. The axis from $\theta = 0^\circ$ to $\theta = 180^\circ$ is discretized into non-equal sized bins. The axis of the cumulative distribution function is given in steps of 0.01° for $0^\circ \leq \theta \leq 2^\circ$, 0.05° for $2^\circ < \theta \leq 5^\circ$, 0.1° for $5^\circ < \theta \leq 10^\circ$, 0.5° for $10^\circ < \theta \leq 15^\circ$, 1° for $15^\circ < \theta \leq 176^\circ$, and 0.25° for $176^\circ < \theta \leq 180^\circ$.

TABLE I. Specifications of the Raman lidar system to be simulated using the Monte Carlo code developed. These specifications are based upon previously demonstrated Raman lidar systems designed for lower atmospheric monitoring and upon a Raman lidar system under development designed for polar deployment.

Beam Diameter	2.7 cm
Beam Divergence	$167\ \mu\text{rad}$
Beam Shape	Top Hat
Laser Energy	0.400 J
Laser Rep Rate	30 Hz
Laser Wavelength	354.75 nm and 532 nm
Pulse Width	$3 - 7\text{ ns}$

This should be considered, for example via the technique of Hokr et al.²⁹, for focused beam

applications but is not necessary in this case as the beam is divergent.

The allowable MPE for direct and indirect exposure, as well as the NOHD and NHZ, is calculated using the ANSI standard equations¹². These results form a set of measurements with which one can compare the calculated results. These standards are summarized in Table II. Because of the ultraviolet wavelength selected, the MPE for single and multiple pulses is relatively high compared to that over the wavelength range from 400 nm to 700 nm. For upper atmospheric lidar systems, the wavelength selection is a trade between the relative scattering cross section and optical transmission efficiency. For this reason, this paper will consider two wavelengths, the 2nd and 3rd harmonic wavelength of an Nd:YAG laser. All system characteristics are held fixed except the wavelength. Note that the conversion from the second to third harmonic is never perfectly efficient and as a result the assumption that the system specifications are identical is non-physical for a single laser source; nevertheless, this assumption is made to facilitate a simple comparison by keeping all factors equal other than wavelength. One can simply scale the Monte Carlo results once calculated for the exact power produced by a particular laser but for demonstration purposes this extra step is not done.

TABLE II. ANSI standard range and energy density calculations based on the worst-case laser system specifications given in Table I and the standards specified in ANSI Z136.1¹². All simulations to be presented will have color bars scaled to the MPE values given here. Exposure duration of 10 seconds is assumed using a factor of 2.5 reduction in MPE for exposure to such systems everyday for 355 nm. The extended source correction is applied to 532 nm wavelength assuming a nominal flight altitude of 500 meters and scattering from anywhere within 4 meters of the exit port (the size of the regions for the simulations run). The direct pulse MPE is used for the NOHD calculation and the indirect for the NHZ calculation.

	$\lambda = 355 \text{ nm}$	$\lambda = 532 \text{ nm}$
Direct Pulse MPE (mJ/cm^2)	4.14	2.0×10^{-4}
Indirect Pulse MPE (mJ/cm^2)	1.33	10.7×10^{-4}
NOHD (km)	0.645	95.7
NHZ (cm)	9.77	345

V. APPLICATION TO POLAR CONDITIONS

In this section the Monte Carlo method is demonstrated in varying atmospheric conditions. The scene to be taken is that of a high-altitude Arctic deployment. Such a location provides unique challenges to lidar deployment and operation but is applicable to other polar locations where the operation of lidar is being conducted or considered (i.e. the South Pole Station). Unlike the Antarctic, the Arctic has the additional safety issues concerning high altitude intercontinental jets and low altitude landing aircraft that routinely fly over the region and may be susceptible to laser hazards from the ground. Additionally, personnel routinely work in and around the systems operational area. In particular, the goal is to ascertain whether local meteorological conditions may create scattering that alters the range where laser light is a hazard for aircraft and staff.

This paper assumes the following scene modeled off of Summit, Greenland, a high altitude field site that is outfitted with several atmospheric lidar systems^{30,31} and has much of the infrastructure required for the assumed system. Summit is a small camp located just south east of a snow runway. Due to the nature of polar research logistics and practical limitations, the camp exists within the laser free zone as defined by ANSI¹³. The beam will propagate vertically through a cylindrical region with radius r measured from the center of the beam, and height, h . The beam energy density at the exit port of the laser is allowed to be in excess of the MPE because it is assumed that the exit port is well quarantined and the onsite staff has received training to avoid direct beam exposure. However, low altitude aircraft flying at a few hundred meters above the ground may be in the vicinity because the station is accessible by a nearby runway. These flights are required to be side-viewing of the beam and not directly in the path. This is reasonable because Summit is an air-sampling site and regulations are in place to avoid contaminating atmospheric measurements with aircraft exhaust. These regulations prevent low altitude direct overflight and implementation of an interlocked surveillance radar provides the additional control to prevent laser illumination of overhead aircraft, including intercontinental flights. Personnel on the ground will be working in and around the beam in all weather conditions but will not be exposed directly to it. Note that the same conditions assumed here may apply to an aircraft-mounted lidar system in flight with possible beam access to the side and at a distance h from the exit port. In both cases, one eliminates direct beam exposure at the exit port of the lidar system as

an operational concern using administrative and physical controls.

A number of frequent meteorological conditions that occur in the high Arctic, including active precipitation, low thick clouds, blowing snow, fog, and clear air, induce scattering conditions that mentioned (ANSI 136.6 Section 3.3.7) but typically neglected in ANSI safety standards (ANSI 136.6 Appendix C4). This paper will examine the impacts of clear air, liquid fog, and blowing snow on the hazard zone definition. These weather conditions span a broad range of hazards that have been observed at Summit³⁰. Danger is maximized to: 1) high aircraft in clear air; 2) low aircraft near fog and blowing snow; and 3) the onsite staff near fog and blowing snow.

In all cases, the distances r and h will be prescribed to determine the energy density caused by the beam at the boundary of the cylindrical region of interest. Simulations can be run to determine where the beam exceeds the MPE; thus, r and h become the hazard zone and ocular hazard distance respectively when the energy density drops below the MPE. These can be compared to the ANSI standards to determine the effect of scattering.

One note that should be stressed is that the results shown are taken from independent data runs. If one were to discretize the layer of interest into concentric cylinders and track the photons traveling through each layer, normalized irradiances can exceed one. This is demonstrated by Bohren and Clothiaux¹⁴ for a two stream Monte Carlo method in their Figure 6.11. The irradiance is defined as the flux of energy per unit area. Allowing for scattering, it is possible for a photon to propagate through a layer, be redirected and propagate back through the same layer. As a result, a photon can be counted twice or more depending on the optical thickness of the layer and the phase function. This enhancement mechanism is considered in the Section VI.

A. Clear Air

A comparison between the simulation developed with the ANSI standards is in order to compare and contrast the differences in the assumed standard scene and the weather observed at Summit. Reproducing the ANSI standards with the same scene and then replicating a more accurate system scene is necessary. The first step taken was to model clear air. Scattering by diatomic nitrogen and oxygen is considered, which, at the wavelengths of the given lidar system, is well modeled by Rayleigh scattering. The Rayleigh phase function

given in Figure 3 is used. The optical depth is converted to distance using a simple scattering model that is a combination of a Rayleigh scattering model and an aerosol model³². This results in an average optical depth per meter of $3.67 \times 10^{-5} m^{-1}$ for the UV calculated over a range of pressures from the surface to 10km above sea level. The atmospheric model from which the pressures are simulated is the US Naval Research Laboratorys Mass Spectrometer and Incoherent Scatter Radar model.

A set of simulations is run with cylindrical regions all of the same radius but with varying heights. A map of Monte Carlo photons per unit optical depth area is calculated, then converted to photons per area using the specified optical depth per meter. Finally, it is converted to energy density by converting the simulated photons to laser photons. This yields a map of energy density as a function of location for each trial. The top of each cylinder is given to demonstrate how energy density is scattered and directly transmitted. This is shown in Figure 6.

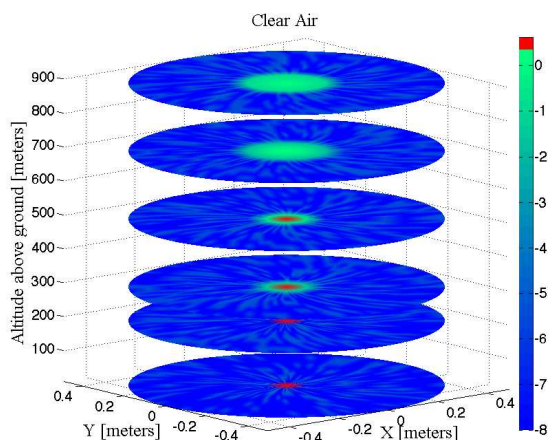


FIG. 6. Energy density of all 355 nm laser radiation at the top of the layer of interest for 6 different altitudes: 10 m , 200 m , 300 m , 500 m , 700 m , 900 m . The color bar is given in log base 10 of the energy density with units of mJ/cm^2 . Note that the red color indicates that the energy density for the hypothetical system with clear air would exceed the single pulse (direct) MPE for the system as modeled.

The side of each cylinder can be treated in the same manner as the tops. The radius varies from the ANSI calculated NHZ to 4 m for 355 nm . This size is chosen to represent distances from the beam outward to the edge of a window which would cover a lidar telescope and

on to the roof of a building where one of the onsite staff could potentially be working. This is shown in Figure 7. In both cases it can be seen that the only hazard is from the direct beam. Even at a wavelength of 355 nm where one expects a significant amount of scattering due to diatomic nitrogen and oxygen, the simulation does not indicate the scattered light to be a hazard.

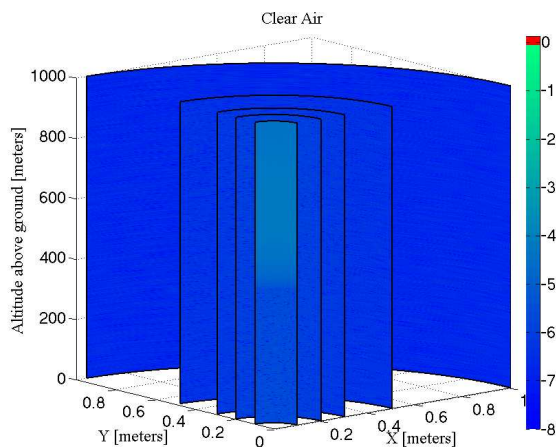


FIG. 7. Clear-air scattered energy density of all 355 nm laser radiation on the side of the layer of interest with 5 different radii: 10 cm , 20 cm , 30 cm , 50 cm , and 100 cm . The color bar is given in log base 10 of the energy density with units of mJ/cm^2 . Note that the red color indicates that the energy density for the hypothetical system with clear air would exceed the indirect MPE for the system as modeled.

It is common for lidar systems to use the visible spectral range for atmospheric applications. As an example, Nd:YAG lasers are simple, robust, readily available, and the second harmonic at approximately 532 nm is a great choice to balance scattering cross section with atmospheric transmission. Furthermore, for autonomous unattended lidar systems the solid-state nature of the lasing medium is favored over, for example, dye lasers. It should be noted that the 532 nm laser propagation analysis below is only an exercise and does not represent the laser operations planned for Summit, which is at 355 nm . The Rayleigh phase function in the visible is nearly identical to that at 355 nm . The optical depth per meter is similar as well but slightly less for the longer wavelength. Both are calculated independently but only the results for 355 nm are given in the interest of brevity. The energy density exiting the side of each cylinder for 532 nm is shown in Figure 8. The results are not repeated for

532 nm range-dependency because the beam is well in excess of the MPE and as such shows little structure.

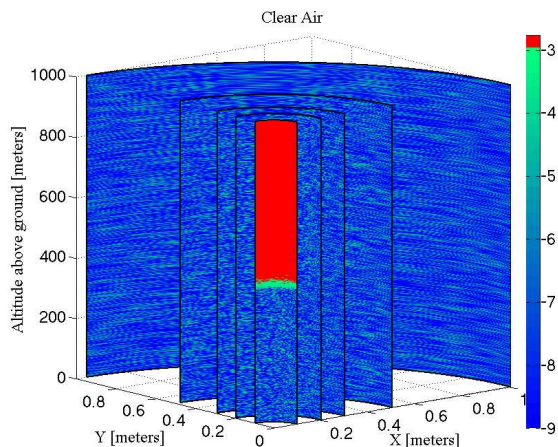


FIG. 8. Clear-air scattered energy density of all 532 nm laser radiation on the side of the layer of interest with 5 different radii which are the same as Figure 7. The color bar is given in log base 10 of the energy density with units of mJ/cm^2 . Note that the red color indicates that the energy density for the hypothetical system with clear air would exceed the indirect MPE for the system as modeled. The MPE for 532 nm is more than 3 orders of magnitude lower than for 355 nm.

B. Liquid Fog

Liquid fog near the start and end of the summer season is a regular occurrence observed at Summit. Low-level fog is frequently observed for several hours after the sun dips below the horizon resulting in relatively cold temperatures compared to the day. Furthermore, much atmospheric research is focused on understanding liquid and mixed phase clouds, both of which occur at Summit³⁰. In either case, liquid drops formed in supersaturated air but with few condensation nuclei are not converted directly to ice via the Wegener/Bergeron/Findeisen process. Although colloidally unstable, liquid water persists in the Arctic throughout the year³³.

This fog causes visibility to drop significantly and provides a good case study for determining laser safety. Here a fog with a liquid water path of $20 g/m^2$ per every 500 m and an effective radius, defined as the third moment of the size distribution divided by the second moment, of fog droplets of $15 \mu m$ is assumed. The conversion of liquid water path to optical

depth in Equation 8 gives optical thickness per meter³⁴; here LWP is the liquid water path, R_e is the particle effective radius, τ is the optical depth, and ρ is the density of liquid water or ice. The assumed liquid water path is based on measurements of the ICECAPS Program (Arctic Observing Network Grant Numbers ARC-0856773, 0904152, and 0856559). This fog is assumed to form at the ground but these assumptions could also be representative of a thin low-level liquid cloud.

$$LWP = \frac{2r_e\tau\rho}{3} \quad (8)$$

Similar to the clear air case, two sets of data runs are presented: one which holds radius fixed, Figure 9, and varies height while the second holds height fixed and varies radius, Figure 10.

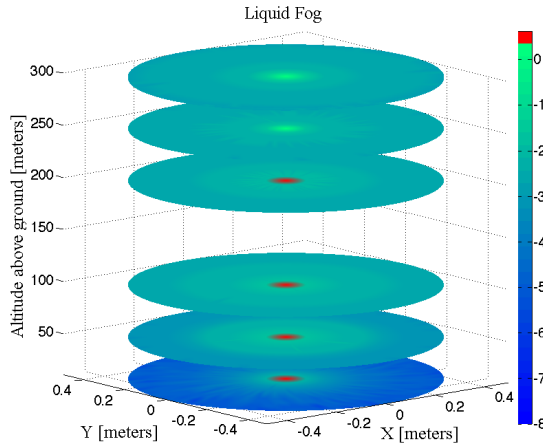


FIG. 9. Fog-scattered energy density of all 355 nm laser radiation at the top of the layer of interest for 6 different altitudes: 10 m , 50 m , 100 m , 200 m , 250 m , 300 m . The color bar is given in log base 10 of the energy density with units of mJ/cm^2 . Note that the red color indicates that the energy density for the hypothetical system with clear air would exceed the direct MPE for the system as modeled.

In comparison to the clear air case, the effective NOHD decreases dramatically from that predicted by the ANSI standards, by a factor of approximately 2.3. However, this is not evident in the radial case because the scattered intensity is not near or in excess of the MPE. However, the same set of results at 532 nm indicates that liquid water fog could present a serious safety risk within 2-3 m of the beam. The results for 532 nm are presented in Figure

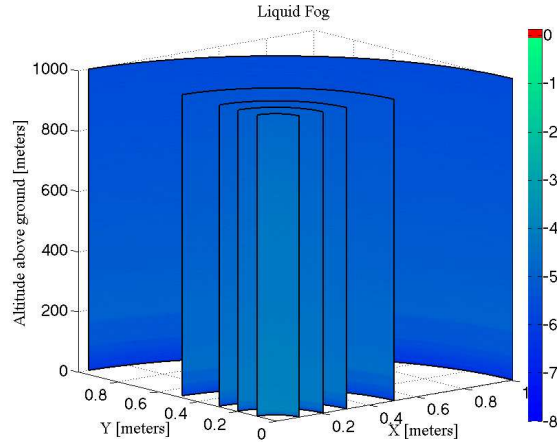


FIG. 10. Energy density of all 355 nm laser radiation on the side of the layer of interest for foggy conditions at the same ranges as Figure 7 and 8. On the scale of the MPE, there is very little energy leaving the side of the layer of interest.

11.

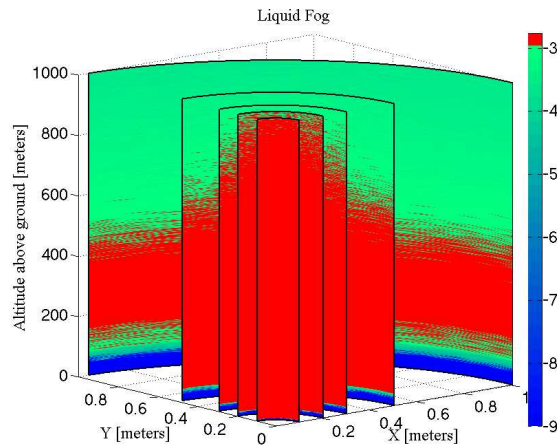


FIG. 11. Fog-scattered energy density of all 532 nm laser radiation on the side of the layer of interest at the same ranges as Figure 7, 8, and 10.

The scattered radiative energy density out of the sides of the regions of interest exceeds the clear air case by at least 2 orders of magnitude. This is to be expected given the relatively large optical depth of fog versus clear air. One can observe that the scattered energy density out the side of the region of interest for fog also shows less uniformity near the ground. Considering that the phase function is sharply forward peaked for liquid water droplets,

this is not surprising. For a photon to leave the layer near the ground, one would expect that scattering near 90° would be approximately 4 orders of magnitude less than that in the forward scattering direction.

C. Blowing Snow

Ice crystals exist suspended in the air above Summit for much of the year. Ice particles can either be precipitated out of clouds as snow or it can be lifted from the surface via wind. Precipitation events are observed throughout the year and occur most frequently during summer³⁰. Furthermore, enhancements in precipitation caused by cloud systems, such as seeder feeder cloud systems where ice crystals from a higher cloud fall through and collect liquid water from a lower, have been observed by the ICECAPS program's polarization lidars. To model this system, the phase function used could be any mix of common ice crystal habits including but not limited to plates, columns, needles, or dendrites. To avoid the complication of having to choose a habit, a mixture of habits is assumed; it is also assumed that the crystals have been roughened²¹. This choice, while limiting in its scope, allows for one to apply the simulations equally to entrained snow as well as that precipitated assuming some riming occurs during the crystals fall time.

Similar results to the case found for liquid water fog for 355 nm were found for blowing snow, Figures 12 and 13. The effective radius of particles is assumed to be $20\ \mu\text{m}$ with the same LWP of $20\ \text{g}/\text{m}^2$ for consistency. With these parameters, one again sees a large difference of the NOHD between the blowing snow and ANSI standards. This is to be expected. The beam energy stays focused for longer due to a combination of slightly smaller optical depth and the more strongly forward peaked phase function.

Again, the scattering of radiation out the side is below the MPE when plotted for 355 nm . However, at 532 nm , the scattered radiation exceeds the MPE. This is shown in Figure 14.

Extending this work to other crystal habits is certainly possible. One simulation, which is interesting is the preferential orientation of ice crystals, which has been observed via ground based polarization lidar³¹ and satellite³⁵. It has been noted that preferential orientation is temperature dependent and that hexagonal plates are a likely habit to orient due to temperature and aerodynamic arguments³⁵. This extension is interesting due to the specular reflections that characterize their scattering interaction but is complicated due to

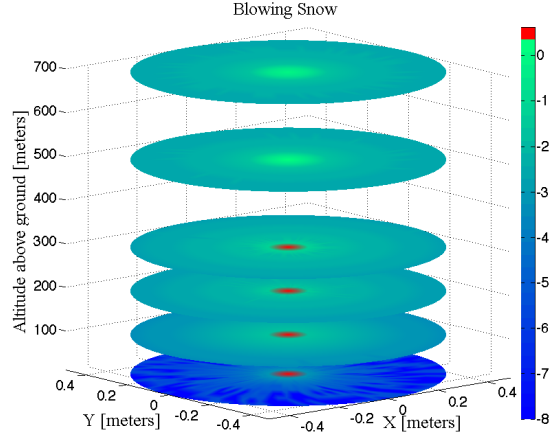


FIG. 12. Snow-scattered energy density of all 355 nm laser radiation at the top of the layer of interest for 6 different altitudes: 10 m , 100 m , 200 m , 300 m , 500 m , 700 m . The color bar is given in log base 10 of the energy density with units of mJ/cm^2 .

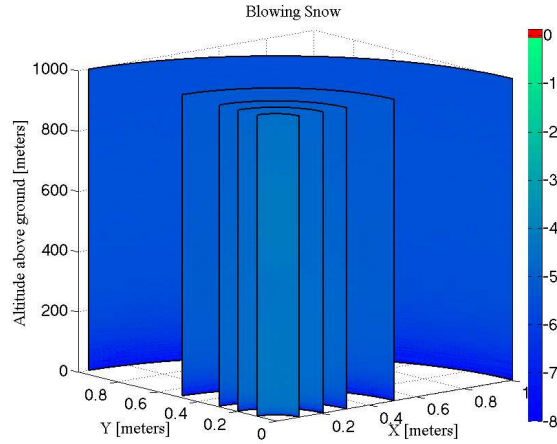


FIG. 13. Snow-scattered energy density of all 355 nm laser radiation on the side of the layer of interest at the same ranges as Figure 7, 8, 10, and 11. The scattered energy at 355 nm is scaled relative to the MPE and shows no danger.

the common assumption of random orientation in geometric optics and T-Matrix codes. To perform this simulation, the scattering regime would have to be represented but would be dependent on the angle of incidence of all scattered photons, which for multiply scattered photons would likely not be normal, as well as the fraction of oriented to non-oriented ice crystals, which is not well understood. As a result, the oriented ice crystal case is beyond

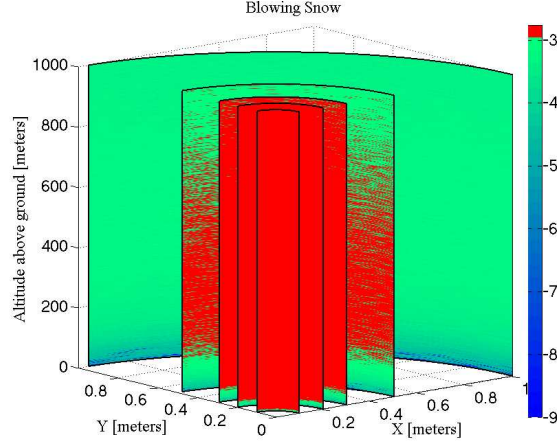


FIG. 14. Snow-scattered energy density of all 532 nm laser radiation on the side of the layer of interest at the same ranges as Figure 7, 8, 10, 11, and 13. The scattered energy at 532 nm is scaled relative to the MPE and shows much more danger than at 355 nm.

the scope of this analysis.

VI. DISCUSSION

Considering the ANSI definitions of the NOHD and the NHZ, these standards are always overestimated. For example, the NOHD is defined in Equation 9¹² in terms of the full divergence angle, ϕ , the beam energy Q , and the beam waist a . A simple rearrangement can help illuminate the underlying physical meaning of this equation, given in Equation 10. This equation is almost exactly the equation for the expansion of the circular beam area as it propagates in vacuum, assuming a small angle approximation for ϕ . The term $\phi NOHD$ represents the amount of growth of the beam assuming ϕ is sufficiently small such that $\tan \phi \approx \phi$.

$$NOHD = \frac{1}{\phi} \sqrt{\frac{4Q}{\pi MPE} - a^2} \quad (9)$$

$$\frac{\pi (\phi^2 NOHD^2 + a^2)}{4} = \frac{Q}{MPE} \quad (10)$$

The vacuum assumption is reasonable for short propagation distances but as the distance increases, the optical depth of the propagation medium grows. The probability of scattering

TABLE III. The distances that a beam needs to travel through the medium of interest to show no more energy density in the forward direction which exceeds the MPE. These values are scaled to the MPE for 355 nm because the beam will become safe below airplane altitudes. As mentioned in the Results section, the 532 nm beam shows little structure because its beam is always in excess of the MPE below aircraft altitudes. OHD stands for ocular hazard distance.

	OHD at 355 nm [meters]	NOHD Difference [%]
ANSI NOHD	645	—
Blowing Snow	430	33.3
Clear Air	626	2.95
Liquid Fog	285	55.81

increases with optical depth thus as propagation distance increases, so too does the probability that beam energy is scattered from the beam. Furthermore, the NOHD equation does not represent the physics of aerosol or cloud scattering. A summary of the propagation distances required for the beam energy density to fall below the MPE is given in Table III.

The NHZ equation can still be used to define the safe radius about the beam but it too can be severely overestimated if the beam energy is attenuated. Here again, there is a problem that is poorly captured within the definition of the NHZ. A simple rearrangement of the definition of NHZ can also yield a form which is essentially an area equaling the laser energy divided by the MPE. This equation will always yield an overestimate of area as well, basically assuming energy is spread by a completely hard target Lambertian scatterer, an idealization which is not physical for atmospheric “soft target” scatterers. A summary of the calculated hazard zone radius to show when the energy density falls below the MPE is given in Table IV.

While over estimating the hazard will ensure that accidental access is not achieved, as laser systems become more mobile, powerful and capable, it is reasonable to question the scale to which safety bounds are overestimated. For the lidar system specified in this work, the overestimate is calculable. For simple molecular scattering, the NOHD estimate is reasonable but for fog, the NOHD is overestimated by nearly a factor of 2.3 higher than observed in this simulation. For the NHZ, the fact that atmospheric scatterers, “soft targets, do not scatter all light and are not Lambertian yields a factor of approximately 18 differ-

TABLE IV. The distance from the beam center that the Monte Carlo results show the energy density of at least one area is in excess of the MPE for 532 [nm]. This calculated distance is compared to the NHZ to determine how close a worker or plane could come to the beam without being exposed to a dangerous energy level. HZ stands for hazard zone.

	HZ at 532 nm [cm]	NHZ Difference [%]
ANSI NHZ	345	—————
Blowing Snow	111	67.8
Clear Air	19	94.5
Liquid Fog	249	27.8

ence between the NHZ calculated with the ANSI standards and those calculated assuming scattering.

The final point of emphasis to be considered is enhancements due to the definition of the region of interest. The results above assume that the region of interest bounds the scattering volume and when the photon leaves, its energy is imparted into that small section of space. This effectively assumes that each section on the exterior of the region of interest can encounter a person. If, however, this assumption is recast and it is assumed that only one person exists to interact with the beam, this assumption is unnecessarily restrictive. It is possible for a photon to leave the region of interest and then return and interact with a completely different region. As a result, enhancement in energy density can be observed. In this case, a photon only leaves the layer of interest out the top or bottom.

A simulation was written to accommodate this condition where the photon is allowed to propagate out the sides and return to the layer of interest. The stopping condition in this case is only when the photon leaves the top and bottom. Then enhancement of energy density of such a condition is considered. The enhancement for all of the cases presented was observed. For clear air, the maximum of the enhancement was less than a percent, 0.23% of the energy density, for liquid water it was 3.58% and for ice it was 3.73%. This corresponds to an enhanced range of the hazard zone presented in Table IV of 4 cm for clear air, 2 cm for liquid water, and 1 cm for blowing snow. As the enhancements for liquid water and blowing snow are spread over a greater surface area, it takes relatively more enhancement to cause changes in distance than does the smaller clear air hazard zone.

VII. SUMMARY

As atmospheric lidar systems become more common and more capable, operational safety concerns must continue to be considered and addressed. This paper addresses the question of how well do the ANSI standard definitions of NOHD and NHZ perform when considering scattering for various atmospheric conditions. It evaluates scattering and confirms that the NOHD and NHZ for randomly oriented atmospheric particles are always conservative. It is noted that the analysis of non-randomly oriented particles might represent a safety hazard beyond the standard NHZ calculation but the calculation is outside the scope of this work, which is designed to demonstrate the Monte Carlo method.

The assumptions used in the calculation of the ANSI standard NOHD and NHZ for vertical beams do not well represent the physical situation of interest for safety analysis of atmospheric lidar. The NOHD for a vertically propagating beam assumes no scattering where the NHZ assumes complete hard target scattering of a beam, but atmospheric scatterers, i.e. “soft targets”, exist somewhere in between these two extremes. This paper has demonstrated a Monte Carlo method to evaluate the hazard zone of an atmospheric lidar for “soft targets” and introduced three case studies of common atmospheric conditions for a high-powered UV Raman lidar designed for polar deployments. It was shown that the hazard zone, where direct or indirect energy from a lidar beam is higher than the allowable MPE propagating through the atmosphere, is inextricably linked to the scattering environment. In particular the hazard zone is strongly linked to the optical thickness of a medium and the prominence of the forward scattering peak of the medium’s phase function. This paper has introduced a flexible Monte Carlo method that can represent arbitrary calculated phase functions and scattering environments without requiring assumption or simplification to model “soft target” environments.

It was found that the NOHD and NHZ are always overestimates of the safe distance from the beam. It was shown that the NOHD is within 3% of the hazard zone assuming clear air scattering only for the system of interest. However for fog or blowing snow, the most common atmospheric mode at Summit, Greenland, the NOHD is an overestimate by 56% and 33% respectively. Conversely, clear air is the softest target considered and differs substantially from the NHZ assumed complete scattering. The NHZ is approximately 95% larger than the hazard zone assuming atmospheric clear air scattering but only 68% and

28% larger for blowing snow and fog.

For future work, some enhancements to the basic Monte Carlo method described should be considered. A major enhancement would be the inclusion of variance reduction techniques to relax the computational expense of the presented simulations, especially statistical estimation^{16–18,36–38}. This would reduce variance and make the described simulations more applicable to problems studied, for example, in backscattered energy density by Megaloudis et al.³⁹.

VIII. ACKNOWLEDGMENT

This material is based upon work supported by the National Science Foundation Graduate Research Fellowship under Grant No. DGE 1144083, National Science Foundation Grant No. AON 1303864 and National Science Foundation Grant No. ATM-0454999. The authors would like to acknowledge Josh Hadler who encouraged us to pursue writing and complete this manuscript. Finally, the authors would like to acknowledge the help of the entire ICECAPS team and specifically Dave Turner who provided insight into liquid water path and effective radius of observed scatterers.

REFERENCES

- ¹T. Fujii, T. Fukuchi (Eds.), *Laser Remote Sensing*, Taylor and Francis Group, 2005.
- ²R. M. Measures, *Laser Remote Sensing: Fundamentals and Applications*, John Wiley and Sons, 1984.
- ³C. Weitkamp (Ed.), *Lidar Range-Resolved Optical Remote Sensing of the Atmosphere*, Vol. 102, Springer, 2005.
- ⁴J. E. M. Goldsmith, F. H. Blair, S. E. Bisson, D. D. Turner, Turn-key raman lidar for profiling atmospheric water vapor, clouds, and aerosols, *Appl. Opt.* 37 (21) (1998) 4979–4990. doi:10.1364/AO.37.004979
URL <http://ao.osa.org/abstract.cfm?URI=ao-37-21-4979>
- ⁵J. Reichardt, U. Wandinger, V. Klein, I. Mattis, B. Hilber, R. Begbie, Ramses: German meteorological service autonomous Raman lidar for water vapor, temperature, aerosol, and cloud measurements, *Appl. Opt.* 51 (34) (2012) 8111–8131. doi:10.1364/AO.51.008111
URL <http://ao.osa.org/abstract.cfm?URI=ao-51-34-8111>
- ⁶S. M. Spuler, K. S. Repasky, B. Morley, D. Moen, M. Hayman, A. R. Nehrir, Field-deployable diode-laser-based differential absorption lidar (dial) for profiling water vapor, *Atmospheric Measurement Techniques* 8 (3) (2015) 1073–1087.
- ⁷P. Di Girolamo, R. Marchese, D. N. Whiteman, B. B. Demoz, Rotational raman lidar measurements of atmospheric temperature in the uv, *Geophysical Research Letters* 31 (1). doi:10.1029/2003GL018342
URL <http://dx.doi.org/10.1029/2003GL018342>

- ⁸R. Eixmann, M. Gerding, J. Höffner, M. Kopp, Lidars with narrow FOV for daylight measurements, *IEEE Transactions on Geoscience and Remote Sensing* 53 (8) (2015) 4548–4553.
- ⁹C. J. Flynn, A. Mendoza, Y. Zheng, S. Mathur, Novel polarization-sensitive micropulse lidar measurement technique, *Opt. Express* 15 (6) (2007) 2785–2790. doi:10.1364/OE.15.002785.
URL <http://www.opticsexpress.org/abstract.cfm?URI=oe-15-6-2785>
- ¹⁰J. P. Thayer, N. B. Nielson, R. E. Warren, C. J. Heinselman, Rayleigh lidar system for middle atmosphere research in the arctic, *Optical Engineering* 36 (7) (1997) 2045–2061.
- ¹¹U. von Zahn et al, The alomar Rayleigh/mie/raman lidar: objectives, configuration, and performance, *Annales Geophysicae* (2000) 815–833.
- ¹²American National Standard for Safe Use of Lasers (ANSI Z136.1), Laser Institute of America, 2014.
- ¹³American National Standard for Safe Use of Lasers Outdoors (ANSI Z136.6), Laser Institute of America, 2015.
- ¹⁴C. F. Bohren, E. E. Clothiaux, *Fundamentals of Atmospheric Radiation*, WILEY-VCH Verlag GmbH and Co. KGaA, 2005.
- ¹⁵P. Bevington, *Data Reduction and Error Analysis for the Physical Sciences*, McGraw-Hill, 1992.
- ¹⁶Bixler, J. N., Hokr, B. H., Winblad, A., Elpers, G., Zollars, B., and Thomas, R. J.: Methods for variance reduction in Monte Carlo simulations, doi:10.1117/12.2213470, URL <http://dx.doi.org/10.1117/12.2213470>, 2016.
- ¹⁷Plass, G. N. and Kattawar, G. W.: Monte Carlo Calculations of Light Scattering from Clouds, *Appl. Opt.*, 7, 415–419, doi:10.1364/AO.7.000415, URL <http://ao.osa.org/abstract.cfm?URI=ao-7-3-415>, 1968.
- ¹⁸Plass, G. N. and Kattawar, G. W.: Reflection of Light Pulses from Clouds, *Appl. Opt.*, 10, 2304–2310, doi:10.1364/AO.10.002304, URL <http://ao.osa.org/abstract.cfm?URI=ao-10-10-2304>, 1971.
- ¹⁹Prahl, S. A., Keijzer, M., Jacques, S. L., and Welch, A. J.: A Monte Carlo Model of Light Propagation in Tissue, *SPIE Proceedings of Dosimetry of Laser Radiation in Medicine and Biology*, IS 5, 102–111, 1989.

- ²⁰Wang, L., Jacques, S. L., and Zheng, L.: MCML—Monte Carlo modeling of light transport in multi-layered tissues, *Computer Methods and Programs in Biomedicine*, 47, 131 – 146, doi:[http://dx.doi.org/10.1016/0169-2607\(95\)01640-F](http://dx.doi.org/10.1016/0169-2607(95)01640-F), URL <http://www.sciencedirect.com/science/article/pii/016926079501640F>, 1995.
- ²¹P. Yang, L. Bi, B. A. Baum, K.-N. Liou, G. W. Kattawar, M. I. Mishchenko, B. Cole, Spectrally consistent scattering, absorption, and polarization properties of atmospheric ice crystals at wavelengths from 0.2 to 100 μ m, *Journal of the Atmospheric Sciences* 70 (1) (2012) 330–347. doi:10.1175/JAS-D-12-039.1. URL <http://dx.doi.org/10.1175/JAS-D-12-039.1>
- ²²T. Binzoni, T. S. Leung, A. H. Gandjbakhche, D. Rufenacht, D. T. Delpy, The use of the heney–greenstein phase function in Monte Carlo simulations in biomedical optics, *Physics in Medicine and Biology* 51 (17) (2006) N313. URL <http://stacks.iop.org/0031-9155/51/i=17/a=N04>
- ²³W. M. Cornette, J. G. Shanks, Physically reasonable analytic expression for the single-scattering phase function, *Appl. Opt.* 31 (16) (1992) 3152–3160. doi:10.1364/AO.31.003152. URL <http://ao.osa.org/abstract.cfm?URI=ao-31-16-3152>
- ²⁴D. Toubanc, Henyey-Greenstein and Mie phase functions in Monte Carlo radiative transfer computations, *Appl. Opt.* 35 (18) (1996) 3270–3274. doi:10.1364/AO.35.003270. URL <http://ao.osa.org/abstract.cfm?URI=ao-35-18-3270>
- ²⁵P. J. Olver, C. Skakiban, *Applied Linear Algebra*, Prentice Hall, 2006.
- ²⁶G. W. Petty, *A First Course in Atmospheric Radiation*, 2nd Edition, Sundog Pub., 2006.
- ²⁷C. F. Bohren, D. R. Huffman, *Absorption and Scattering of Light by Small Particles*, WILEY-VCH Verlag GmbH and Co. KGaA, 1998.
- ²⁸S. Warren, Optical constants of ice from the ultraviolet to the microwave, *Applied Optics* 23 (8) (1984) 1206–1225.
- ²⁹Hokr, B. H., Bixler, J. N., Elpers, G., Zollars, B., Thomas, R. J., Yakovlev, V. V., and Scully, M. O.: Modeling focusing Gaussian beams in a turbid medium with Monte Carlo simulations, *Opt. Express*, 23, 8699–8705, doi:10.1364/OE.23.008699, URL <http://www.opticsexpress.org/abstract.cfm?URI=oe-23-7-8699>, 2015.
- ³⁰M. D. Shupe, D. D. Turner, V. P. Walden, R. Bennartz, M. P. Cadeddu, B. B. Castellani, C. J. Cox, D. R. Hudak, M. S. Kulie, N. B. Miller, R. R. Neely, W. D. Neff, P. M.

- Rowe, High and dry: New observations of tropospheric and cloud properties above the greenland ice sheet, *Bulletin of the American Meteorological Society* 94 (2) (2012) 169–186. doi:10.1175/BAMS-D-11-00249.1.
 URL <http://dx.doi.org/10.1175/BAMS-D-11-00249.1>
- ³¹R. R. Neely, M. Hayman, R. Stillwell, J. P. Thayer, R. M. Hardesty, M. O’Neill, M. D. Shupe, C. Alvarez, Polarization lidar at Summit, Greenland for the detection of cloud phase and particle orientation, *Journal of Atmospheric and Oceanic Technology* doi:10.1175/JTECH-D-12-00101.1.
 URL <http://dx.doi.org/10.1175/JTECH-D-12-00101.1>
- ³²R. J. Pressley, *Handbook of Lasers*, The Chemical Rubber Company, 1971.
- ³³H. Morrison, G. de Boer, G. Feingold, J. Harrington, M. D. Shupe, K. Sulia, Resilience of persistent Arctic mixed-phase clouds, *Nature Geoscience* 5 (1) (2012) 11–17.
 URL <http://dx.doi.org/10.1038/ngeo1332>
- ³⁴J. Bendix, A satellite-based climatology of fog and low-level stratus in Germany and adjacent areas, *Atmospheric Research* 64 (1–4) (2002) 3 – 18, 2nd International Conference on Fog and Fog Collection. doi:[http://dx.doi.org/10.1016/S0169-8095\(02\)00075-3](http://dx.doi.org/10.1016/S0169-8095(02)00075-3).
 URL <http://www.sciencedirect.com/science/article/pii/S0169809502000753>
- ³⁵V. Noel, H. Chepfer, A global view of horizontally oriented crystals in ice clouds from cloud-aerosol lidar and infrared pathfinder satellite observation (CALIPSO), *Journal of Geophysical Research: Atmospheres* 115 (D4). doi:10.1029/2009JD012365.
 URL <http://dx.doi.org/10.1029/2009JD012365>
- ³⁶K. E. Kunkel and J. A. Weinman, Monte Carlo Analysis of Multiply Scattered Lidar Returns. *J. Atmos. Sci.* 33, 1772-1781, (1976)
- ³⁷L. R. Poole, D. D. Venable, and J. W. Campbell, Semianalytic Monte Carlo radiative transfer model for oceanographic lidar systems, *Appl. Opt.* 20, 3653-3656 (1981)
- ³⁸L. R. Poole, Computed laser backscattering from turbid liquids: comparison with laboratory results, *Appl. Opt.* 21, 2262-2264 (1982)
- ³⁹Megaloudis, George, Edward Early, and Paul Kennedy. "Exposure to Backscattered Laser Radiation." *Journal of Directed Energy* 3.4 (2010)